NANO · MICRO small
www.small-journal.com

Bi_2S_3–In_2S_3 Heterostructures for Efficient Photoreduction of Highly Toxic Cr^{6+} Enabled by Facet-Coupling and Z-Scheme Structure

Linjuan Wang, Siva Karuturi, and Ling Zan**

The construction of Z-scheme photocatalyst materials mimicking the natural photosynthesis system provides many advantages, including increased light harvesting, spatially separated reductive and oxidative active sites and strong redox ability. Here, a novel Bi_2S_3 nanorod@In_2S_3 nanoparticle heterojunction photocatalyst synthesized through one-pot hydrothermal method for Cr^{6+} reduction is reported. A systematic investigation of the microstructural and compositional characteristics of the heterojunction catalyst confirms an intimate facet coupling between (440) crystal facet of In_2S_3 and (060) crystal facet of Bi_2S_3, which provides a robust heterojunction interface for charge transfer. When tested under visible-light irradiation, the Bi_2S_3–In_2S_3 heterojunction photocatalyst with 15% Bi_2S_3 loading content achieves the highest Cr^{6+} photoreduction efficiency of nearly 100% with excellent stability, which is among the best-reported performances for Cr^{6+} removal. Further examination using optical, photoelectrochemical, impedance spectroscopy, and electron spin resonance spectroscopy characterizations reveal greatly improved photogenerated charge separation and transfer efficiency, and confirm Z-scheme electronic structure of the photocatalyst. The Z-scheme Bi_2S_3–In_2S_3 photocatalyst demonstrated here presents promise for the removal of highly toxic Cr^{6+}, and could also be of interest in photocatalytic energy conversion.

1. Introduction

In the last few decades, rapid industrialization of electroplating, leather making, and pigment processing technologies has led to the release of increasing amounts of Cr^{6+} into the environment, which is defined as one of most toxic pollutants by the United States Environmental Protection Agency due to its high solubility.[1–3] With 100 times higher toxicity than Cr^{3+}, Cr^{6+} poses a great threat to the ecosystem, particularly from its biological recycling.[4] Thus the concentration of Cr^{6+} in industrial wastewater needs to be strictly controlled before it can be safely discharged. Many methods such as bioremediation, chemical reduction, and physical reverse osmosis have been developed to treat Cr^{6+} in wastewater, but they suffer from high costs.[5–7] Photocatalytic Cr^{6+} reduction has emerged as an attractive direction due to its potential to be environmental friendly, cheap, and sustainable.[1,8] Various photocatalysts have been reported for Cr^{6+} reduction, including phlo-@POF,[9] Cu_2O/TiO_2,[10] Zn(Ce, Mn)-MOFs,[11] $ZnWO_4$,[5] SnS_2–In_2S_3,[12] and $Gd(OH)_3$.[6] However, many of the reported materials show limited photocatalytic efficiency due to their wide bandgaps limiting their light absorption ability and/or inefficient redox ability due to fast recombination of photogenerated electron–hole pairs. The two most promising approaches to address these limitations are the use of narrow bandgap photocatalysts and the adoption of Z-scheme photocatalyst structure.[13] While the former approach enhances the light-harvesting efficiency by extending light absorption beyond the UV region of the solar spectrum, the latter approach offers well-preserved redox ability by spatially separating the reductive and oxidative active sites, mimicking the natural photosynthesis system.

In_2S_3 is an n-type semiconductor and has been widely investigated for various light-driven energy conversion reactions such as water splitting,[14] CO_2 reduction,[15] and N_2 fixation[16] due to its narrow bandgap (2.0–2.2 eV), good chemical stability, appropriate conduction band edge position, and high photoconductivity and photosensitivity.[17] For example, Huang et al. fabricated Ag_3PO_4/In_2S_3 nanocomposites which showed superior photocatalytic efficiency toward the degradation of organic pollutants under visible-light irradiation.[18] Similarly, Wang and co-workers successfully synthesized and demonstrated Yb^{3+}/Tm^{3+} co-doped In_2S_3 with higher photocatalytic activity for Cr^{6+} reduction and rhodamine B oxidative degradation.[19] Bi_2S_3 is another transition metal sulfide similar to In_2S_3

L. Wang, S. Karuturi
School of Engineering
The Australian National University
Canberra, ACT 2601, Australia
E-mail: siva.karuturi@anu.edu.au
L. Wang, L. Zan
College of Chemistry and Molecular Science
Wuhan University
Wuhan 430072, P. R. China
E-mail: irlab@whu.edu.cn
S. Karuturi
Department of Electronic Materials Engineering
Research School of Physics
the Australian National University
Canberra, ACT 2601, Australia
The ORCID identification number(s) for the author(s) of this article can be found under https://doi.org/10.1002/smll.202101833.

DOI: 10.1002/smll.202101833

with a narrow bandgap (≈1.3 eV), can be synthesized with good crystallinity through facile one-pot hydrothermal method, and was demonstrated to form heterojunction with In_2S_3.[20,21] For instance, Fu et al. fabricated hierarchical Bi_2S_3 nanoflower/In_2S_3 nanosheet composites with high visible-light photocatalytic activity through a one-step synthesis method.[22] Similarly, hierarchical Bi_2S_3/In_2S_3 core–shell microspheres were fabricated by Fu and co-workers through growth rate controlled process with enhanced photocatalytic activity.[23] Despite these examples showing great potential of In_2S_3 and Bi_2S_3 for photocatalysis, there are no reports on the fabrication of Bi_2S_3–In_2S_3 heterojunction formation through intimate facet-coupling, and more importantly realizing a Z-scheme photocatalyst based on the two materials.

Herein, a series of Bi_2S_3–In_2S_3 Z-scheme heterostructures are successfully synthesized by one-pot hydrothermal method for Cr^{6+} reduction with facet-coupling between (440) crystal facet of In_2S_3 and (060) crystal facet of Bi_2S_3. The intimate contact at the heterojunction ensures a robust interface for electron transfer and higher charge carrier separation efficiency. Electron spin resonance characterizations and band structure analysis further testify that electrons from the conduction band of Bi_2S_3 transfer directly to the valence band of In_2S_3 confirming a Z-scheme photocatalytic mechanism. Among various heterostructure samples prepared, 15% Bi_2S_3–In_2S_3 sample shows the highest photocatalytic efficiency for Cr^{6+} removal. These findings reveal a significant potential of the Z-scheme Bi_2S_3–In_2S_3 heterostructures for application in photocatalytic environmental remediation and energy conversion.

2. Results and Discussion

2.1. Synthesis and Microstructural Characterization

The X-ray diffraction (XRD) spectra of the Bi_2S_3, In_2S_3, and Bi_2S_3–In_2S_3 heterostructures with different loading amounts of Bi_2S_3 are shown in **Figure 1**. The spectrum of the as-prepared In_2S_3 sample exhibits characteristic peaks located at 13.98, 27.53, 33.39, 47.91 corresponding to the crystal planes of (111), (311), (400), (440) of In_2S_3, which match well with the standard JCPDS card no. 32-0456.[23,24] The pattern of Bi_2S_3 exhibits good crystallinity which is beneficial for efficient electron–hole separation. The characteristic XRD peaks of Bi_2S_3 positioned at 24.93, 28.61, 31.66, 32.94, 33.92, 35.58, 45.55, 48.27, 52.62, 59.1, 59.51 are attributable to the crystal planes of (130), (211), (040), (301), (311), (240), (002), (060), (351), (242), (640) of Bi_2S_3 (JCPDS No. 17-0320), respectively.[25] Besides, no unidentified peaks are observed for In_2S_3 and Bi_2S_3 samples, indicating high purities. The XRD patterns of Bi_2S_3–In_2S_3 heterojunction samples exhibit the characteristic peaks of both In_2S_3 and Bi_2S_3, indicating all the composite samples are composed of both Bi_2S_3 and In_2S_3. In addition, with increasing loading content of Bi_2S_3 in the composite, the intensities of the peaks corresponding to Bi_2S_3 also increase gradually. On the other hand, the peaks that correspond to In_2S_3 are also found to increase, which could be attributed to the role of Bi_2S_3 precursor in promoting the crystal growth of In_2S_3. These results suggest that Bi_2S_3–In_2S_3 heterostructures are successfully synthesized through a facile one-pot hydrothermal synthesis. Interestingly, the characteristic peak

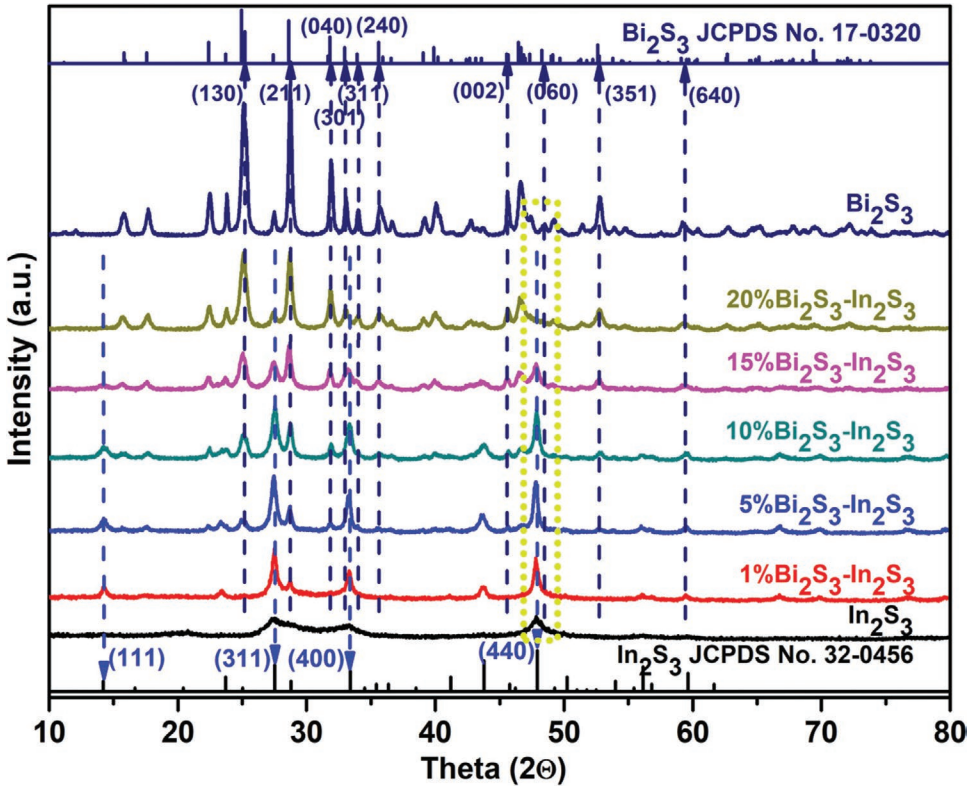

Figure 1. XRD patterns of In_2S_3, Bi_2S_3, and Bi_2S_3–In_2S_3 nanostructures.

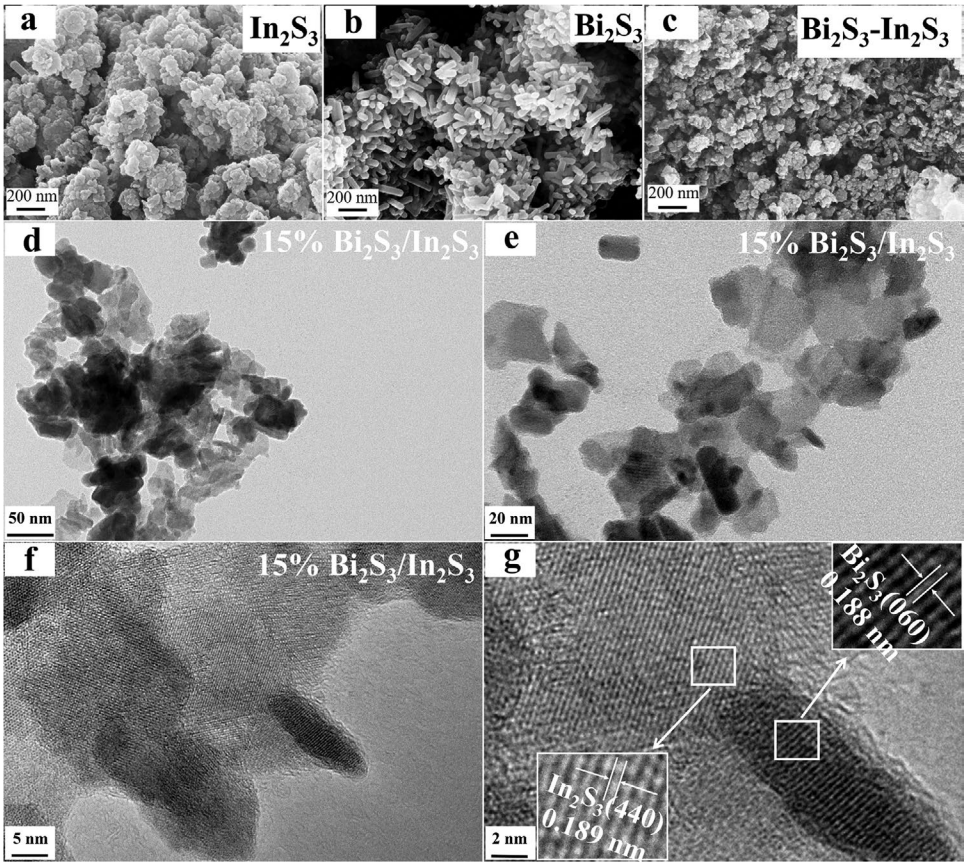

Figure 2. FESEM images of a) In_2S_3, b) Bi_2S_3, and c) Bi_2S_3–In_2S_3 heterostructures. d,e) TEM images of Bi_2S_3–In_2S_3 heterostructures. f,g) HRTEM images of Bi_2S_3–In_2S_3 heterostructure and the lattice fringes of Bi_2S_3 and In_2S_3 (shown as insets in Figure 2g).

located at 48.27 corresponding to (060) crystal plane of Bi_2S_3 disappears in the Bi_2S_3–In_2S_3 heterostructures while a large increase is observed in the intensity of the peak positioned at 47.91 which is attributable to In_2S_3 (440) crystal plane. This can be explained by a possible facet-coupling occurring between (060) crystal plane of Bi_2S_3 and (440) crystal plane of In_2S_3, in agreement with similar observations previously reported in the literature.[26]

The morphology of the as-prepared In_2S_3, Bi_2S_3, and Bi_2S_3–In_2S_3 heterostructure samples were observed through field emission scanning electron microscopy (FESEM) as shown in **Figure 2**a–c. The In_2S_3 displays clusters of nanoparticles with an average diameter ≈25 nm, which is consistent with the reported literature,[27] whereas Bi_2S_3 presents a regular nanorod structure with a length of ≈200 nm and a width of ≈20 nm.[28,29] As for the Bi_2S_3–In_2S_3 heterostructures, a mixed morphology with intimately contacted nanoparticles and nanorods is observed, indicating the Bi_2S_3–In_2S_3 heterostructures were successfully constructed. Moreover, the size of Bi_2S_3 nanorods appears to be smaller than that observed for pristine Bi_2S_3 nanorods. This could be due to the existence of In_2S_3 which prevents the crystal growth of Bi_2S_3. This is also consistent with the XRD results showing the characteristic peak intensities of Bi_2S_3 in the Bi_2S_3/In_2S_3 composites are weaker compared to that of pristine Bi_2S_3. To further investigate the contact interface of In_2S_3 and Bi_2S_3, the samples were characterized using high-resolution transmission electron microscopy (HRTEM). As shown in Figure 2d,e, both In_2S_3 nanoparticles and Bi_2S_3 nanorods exist in close contact with each other which is further confirmed in Figure 2f. Besides, the TEM images suggest the diameter of In_2S_3 is ≈25 nm, while the size of Bi_2S_3 in the composite is much smaller than pristine Bi_2S_3 matching with the SEM observations (Figure 2b). From Figure 2f, a clear interface between In_2S_3 nanoparticles and Bi_2S_3 nanorods can be observed. To confirm the crystal facets at the contact interface, the composite samples were characterized using HRTEM. As shown in Figure 2g, the spacing of lattice fringes on the nanoparticle is 0.189 nm which corresponds to (440) crystal plane of In_2S_3 (JCPDS No. 32-0456), while the nanorod structure exhibits a lattice fringe spacing of 0.188 nm which corresponds to (060) crystal plane of Bi_2S_3 (JCPDS No. 17-0320). Therefore, the HRTEM analysis not only confirms the existence of a robust interface of the Bi_2S_3–In_2S_3 heterojunction, but also reveals a facet-coupling of crystal planes of In_2S_3 (440) and Bi_2S_3 (060), which is also in consistent with the XRD result.

In addition, (060) crystal plane of Bi_2S_3 exposes a large atomic spacing of 3.98 Å between Bi^{3+} and Bi^{3+} according to the crystallographic information file (cif) and the literature.[30] At the same time, the (440) crystal plane of In_2S_3 also exposes a large atomic spacing of 4.04 Å between S^{2-} and S^{2-}.[31] This makes the bonding between (440) crystal plane of In_2S_3 and (060) crystal plane of Bi_2S_3 highly feasible. Based on the above

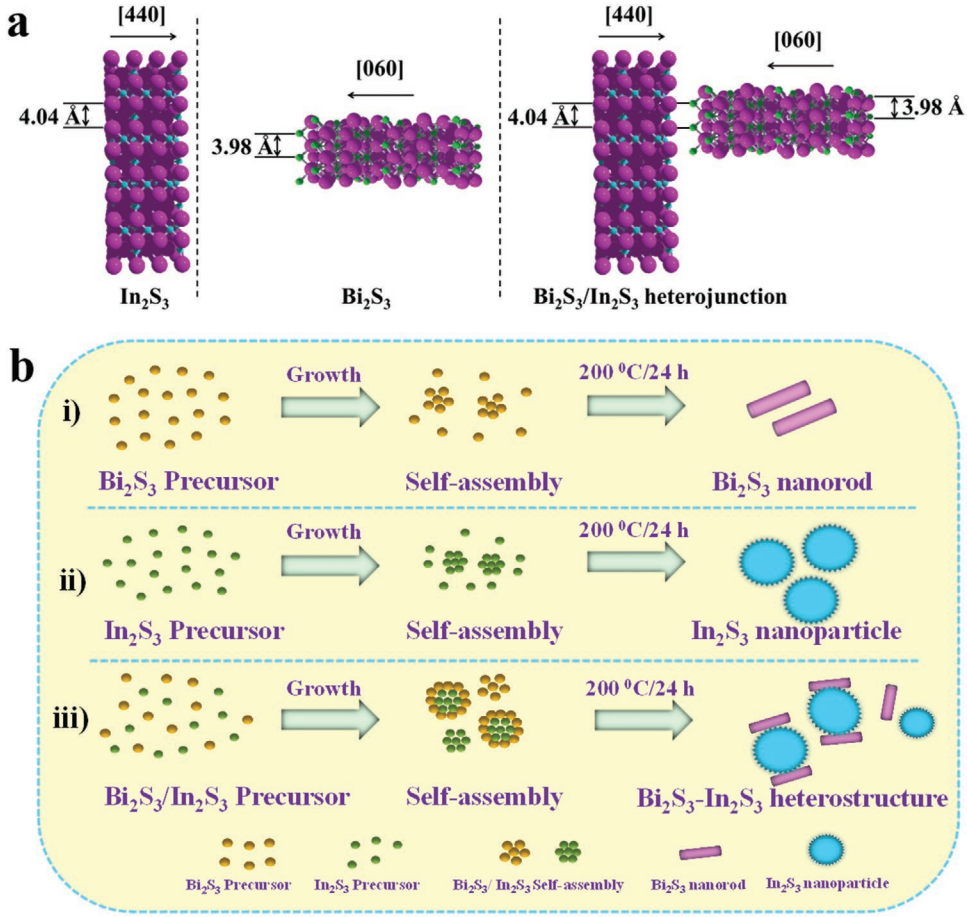

Figure 3. a) The atomic spacing illustration of In_2S_3 (440) and Bi_2S_3 (060) and the contact interface between In_2S_3 (440) and Bi_2S_3 (060). b) Illustration of the growth mechanism of (i) Bi_2S_3 nanorod, (ii) In_2S_3 nanoparticle, and (iii) Bi_2S_3–In_2S_3 heterostructure.

analysis, the proposed crystal structure model and the interfacial bonding of Bi_2S_3–In_2S_3 heterostructure are illustrated in **Figure 3**a. A more detailed atomic distribution information is shown in Figure S2 (Supporting Information).

Based on the comprehensive XRD, SEM, and TEM analyses, we propose a possible growth mechanism of Bi_2S_3 nanorod/In_2S_3 heterostructure as illustrated in Figure 3b. First, upon the ionization of $Bi(NO_3)_3$ and thioacetamide precursors, the cations and anions self-assemble to form a homogeneous distribution of ionic species. Subsequently, upon hydrothermal heating, the isomerization of thioacetamide takes place below 200 °C. The generated isothioacetamide undergoes a strong nucleophilic substitution with Bi^{3+} cations in the mixed solution, which further reacts with S^{2-} anions to form Bi_2S_3 nanorods at 200 °C for 24 h,[32] as shown in step (i) in Figure 3b. The formation process of In_2S_3 nanoparticles is similar to that of Bi_2S_3, as illustrated in step (ii) in Figure 3b. When $Bi(NO_3)_3$, $In(CH_3COO)_2$ and thioacetamide precursors are added together in the solution, bismuth sulfide nuclei and indium sulfide nuclei distribute uniformly in the solution. The Bi^{3+} of bismuth sulfide nuclei adsorbs negatively charged S^{2-} to form S^{2-}-Bi_2S_3 species through electrostatic interactions.[33] This is followed by the formation of In_2S_3–Bi_2S_3 due to the bonding of S^{2-}–Bi_2S_3 with In^{3+} ions originating from indium acetate.[29]

2.2. Composition and Band Structure Analysis

To understand the elemental composition, In 3d, Bi 4f, and S 2s spectra of pristine In_2S_3, Bi_2S_3 and 15% Bi_2S_3–In_2S_3 were analyzed. As illustrated in **Figure 4**a, the X-ray electron spectroscopy (XPS) survey spectra confirm the existence of In, S, and Bi in Bi_2S_3–In_2S_3 heterostructure sample. There are no unidentified elements in pristine In_2S_3 and Bi_2S_3 indicating high purities of the samples. In 3d spectra (Figure 4b) of In_2S_3 and Bi_2S_3–In_2S_3 heterostructure both exhibit two symmetrical peaks at 452.2 and 444.6 eV, confirming the presence of In^{3+} in the In_2S_3 and Bi_2S_3–In_2S_3. No peak shifts are observed between the two samples indicating that interface contacting does not occur through In element. Bi 4f XPS spectra (Figure 4c) of Bi_2S_3–In_2S_3 heterostructure show two characteristic peaks with binding energies at 163.4 and 158.1 eV, which are attributable to Bi^{3+} in the heterostructure. Compared to the pristine Bi_2S_3 with Bi 5f peaks at 163.5 and 158.2 eV, the Bi^{3+} peak of the heterostructure presents a binding energy

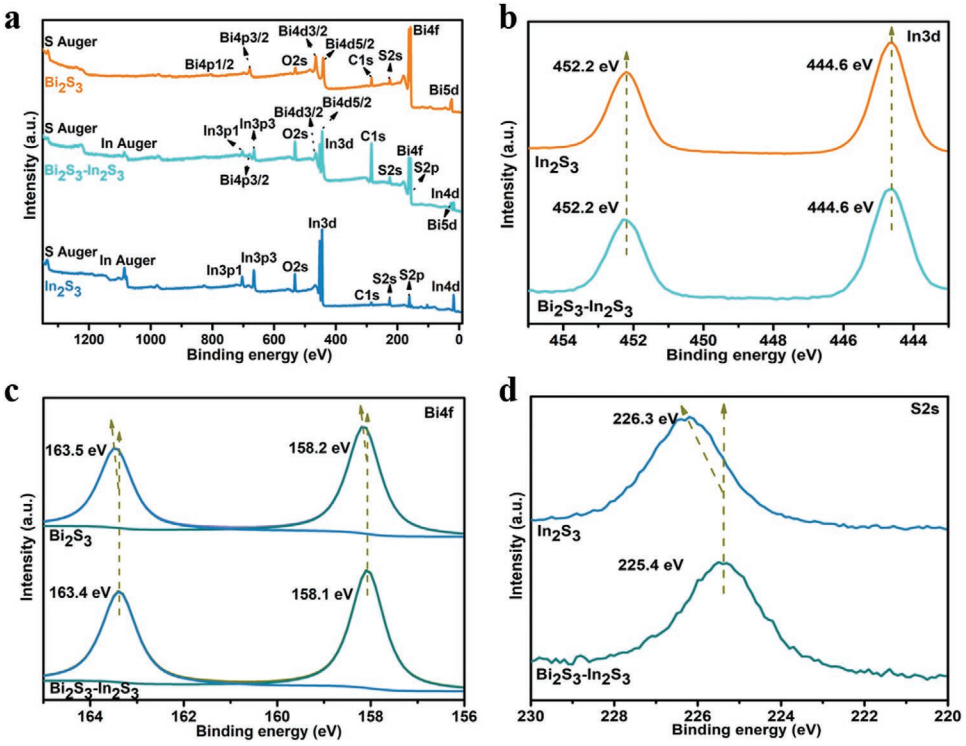

Figure 4. a) XPS spectra of pristine Bi_2S_3, Bi_2S_3–In_2S_3 heterostructure and pristine In_2S_3. b) Comparison of In 3d XPS spectra of Bi_2S_3–In_2S_3 heterostructure and pristine In_2S_3. c) Comparison of Bi 4f XPS spectra of Bi_2S_3–In_2S_3 heterostructure and pristine Bi_2S_3. d) Comparison of S 2s XPS spectra of pristine In_2S_3 and Bi_2S_3–In_2S_3 heterostructure.

peak shift which indicates that the interface contacting occurs through Bi element. The S 2s XPS spectrum (Figure 4d) of Bi_2S_3–In_2S_3 exhibits a characteristic peak at 225.4 eV which shows a binding energy shift compared to the pristine In_2S_3 (226.3 eV). This further substantiates that S element of In_2S_3 binds with Bi_2S_3 at the interface instead of In element. This result is consistent with the schematic illustration presented in Figure 3a.

To investigate the band structure alignment of Bi_2S_3–In_2S_3 heterostructure, Tauc plots, XPS valence spectra were obtained as shown in **Figure 5**. The Tauc plot of In_2S_3 (Figure 5a) intercepts the X-axis at 2.04 eV, indicating 2.04 eV as the bandgap (E_g) value of In_2S_3. At the same time, the Tauc plot of Bi_2S_3 (Figure 5b) shows that the bandgap of Bi_2S_3 is 1.32 eV. An extrapolation of the XPS valence spectra (Figure 5c) intersects with X-axis at the banding energy at 1.21 eV, which corresponds to the valence band position (E_{VB}) of In_2S_3. According to the equation $E_{CB} = E_g - E_{VB}$, the conduction band position (E_{CB}) of In_2S_3 can be calculated as -0.83 eV.

The energy band position of Bi_2S_3 can be calculated using the formulae: $E_{CB} = X - E_0 - 0.5\ E_g$; $E_{VB} = E_{CB} + E_g$. Here, E_0 is the electron free energy on hydrogen scale (4.5 eV), X is the absolute electronegativity of the component atoms.[34] The X value of Bi_2S_3 is 5.56 eV according to the literature,[35] the calculated valence band of Bi_2S_3 (1.72 eV) is much more positive than that of In_2S_3 (1.21 eV),[35] while the conduction band position of Bi_2S_3 can be determined as 0.4 eV which is far more positive than that of In_2S_3 (-0.83 eV),[35] but closer to the valence band of In_2S_3 favoring Z-scheme heterojunction formation. The relative band structure alignment of the heterostructure is illustrated in Figure 5d.

2.3. Photocatalytic Performance for Cr^{6+} Removal

To evaluate the photocatalytic efficiency of the fabricated samples, wastewater treatment for Cr^{6+} reduction was examined as shown in **Figure 6**a with a controlled amount of photocatalyst under visible light irradiation for 30 min. A Cr^{6+} concentration of 20 ppm and a catalyst loading of 0.2 mg mL^{-1} were chosen for the photoreduction experiments. While the Cr^{6+} concentration is comparable to that used in previous works (**Table 1**), we found that a further increased concentration leads to not only an increased adsorption but also a fluctuation of adsorbance from sample to sample. It is also noted that catalyst loading employed in our work is much lower compared to other reported works. While the pristine In_2S_3 sample exhibits a photoreduction efficiency of ≈30%, the pristine Bi_2S_3 photocatalyst exhibits a much lower value ≈2.3% which could be due to its excessively narrow bandgap. On the other hand, all the heterostructure samples exhibit a much higher photocatalytic activity, with the 15% sample showing the best activity which is about 3 times and 44 times higher than that of pristine In_2S_3 and Bi_2S_3 photocatalysts. With the increase in Bi_2S_3 content, the photocatalytic efficiency enhanced gradually reaching 100% at 15% loading. However, the activity decreased when the loading content is increased above 15%, indicating that an optimum ratio of Bi_2S_3 is crucial towards realizing the best photocatalytic

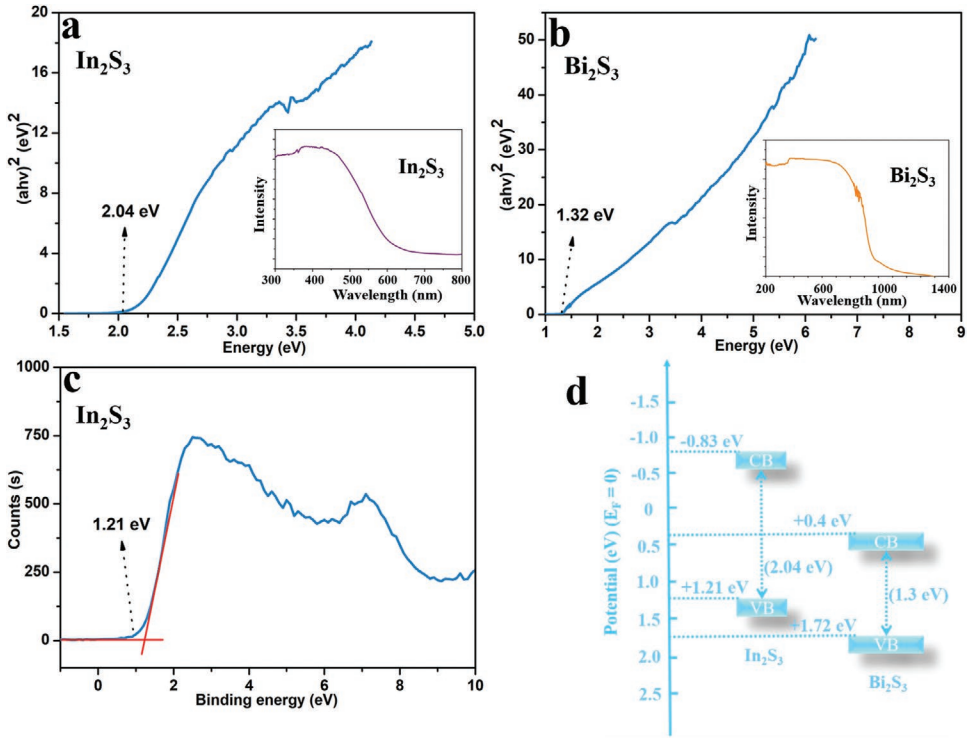

Figure 5. a,b) Tauc plots for In_2S_3 and Bi_2S_3. c) XPS valence spectrum of In_2S_3. d) Schematic illustration of the proposed energy-level alignment in Bi_2S_3–In_2S_3 heterostructure.

activity. The excessive Bi_2S_3 not only can lead to higher electron–hole recombination decreasing the electron utilization efficiency, but could also influence the light absorption of In_2S_3 resulting in shading effect.

The activity of recycled photocatalysts shown in Figure 6b indicates that Bi_2S_3–In_2S_3 sample shows no significant performance degradation for Cr^{6+} reduction after five cycles under visible light irradiation with >96% efficiency maintained, indicating its good photo- and chemical stability. Moreover, as shown in Table 1, the Bi_2S_3–In_2S_3 photocatalyst presents a greater efficiency for Cr^{6+} removal compared to the other previously reported photocatalysts despite a lower catalyst concentration and a shorter reaction time applied in this work, indicating its excellent potential for Cr^{6+} removal. The reproducibility of the photoreduction performance has been verified by repeating the experiments. The as-synthesized catalyst consistently yielded 100% reduction. On the other hand, the recycled catalysts after five runs of recycling yielded the reduction efficiencies of 96.36%, 96.05%, and 96.23% with a standard deviation of 0.16. These results confirm that the catalyst has both good performance and reproducibility.

UV–vis diffuse reflectance spectra (DRS) spectra were collected to examine the light absorption properties of the as-synthesized photocatalyst samples. As shown in Figure 6c, the pristine In_2S_3 exhibits a clear absorption edge at around 620 nm, corresponding to a bandgap energy of 2.0 eV.[39] The absorption edge of Bi_2S_3 is located at around 940 nm (Figure 5b, inset), corresponding to a bandgap of 1.32 eV.[20] The Bi_2S_3–In_2S_3 heterostructures exhibit enhanced light absorption ability than pristine In_2S_3. With increasing Bi_2S_3 content, the light absorption intensity also increases, indicating that the heterostructure sample has an improved light absorption compared to pristine In_2S_3. From the photoluminescence (PL) spectra shown in Figure 6d, pristine In_2S_3 shows the highest PL intensity compared with the heterojunction catalysts, implying a higher electrons–hole recombination. After modifying with Bi_2S_3, all the heterojunction samples show a reduced PL intensity with 15% Bi_2S_3–In_2S_3 sample displaying the weakest peak which is in consistent with the photoreduction activity result. The PL results imply that the addition of Bi_2S_3 reduces the charge carrier recombination in the heterojunction samples leading to higher redox activity.

The transient photocurrent spectra displayed in Figure 6e indicates that all the Bi_2S_3 modified heterojunction photocatalysts show higher photocurrent density than pristine In_2S_3, because of much lower charge carrier recombination in the Bi_2S_3–In_2S_3 heterojunction samples. Electrochemical impedance spectroscopy (EIS) of In_2S_3 and Bi_2S_3–In_2S_3 heterojunction was carried out to analyze the interfacial charge transfer characteristics as shown in Figure 6f. The Bi_2S_3–In_2S_3 heterojunction exhibits a much smaller arc size compared with pristine In_2S_3. The Nyquist plot was also fitted with the equivalent Randle circuit (inset in Figure 6f), where R_s is the electrolyte solution resistance, CPE is the constant phase element for the electrode and electrolyte interface, and R_{ct} is the interfacial charge transfer resistance between the semiconductor and electrolyte.[40] The fitted R_{ct} values for In_2S_3 and 15% Bi_2S_3–In_2S_3 samples in dark are 1.92×10^7 and 9.15×10^6 Ω, respectively. The lower R_{ct} value 15% Bi_2S_3–In_2S_3 confirms a higher charge carrier separation efficiency at the semiconductor/electrolyte interface.[40]

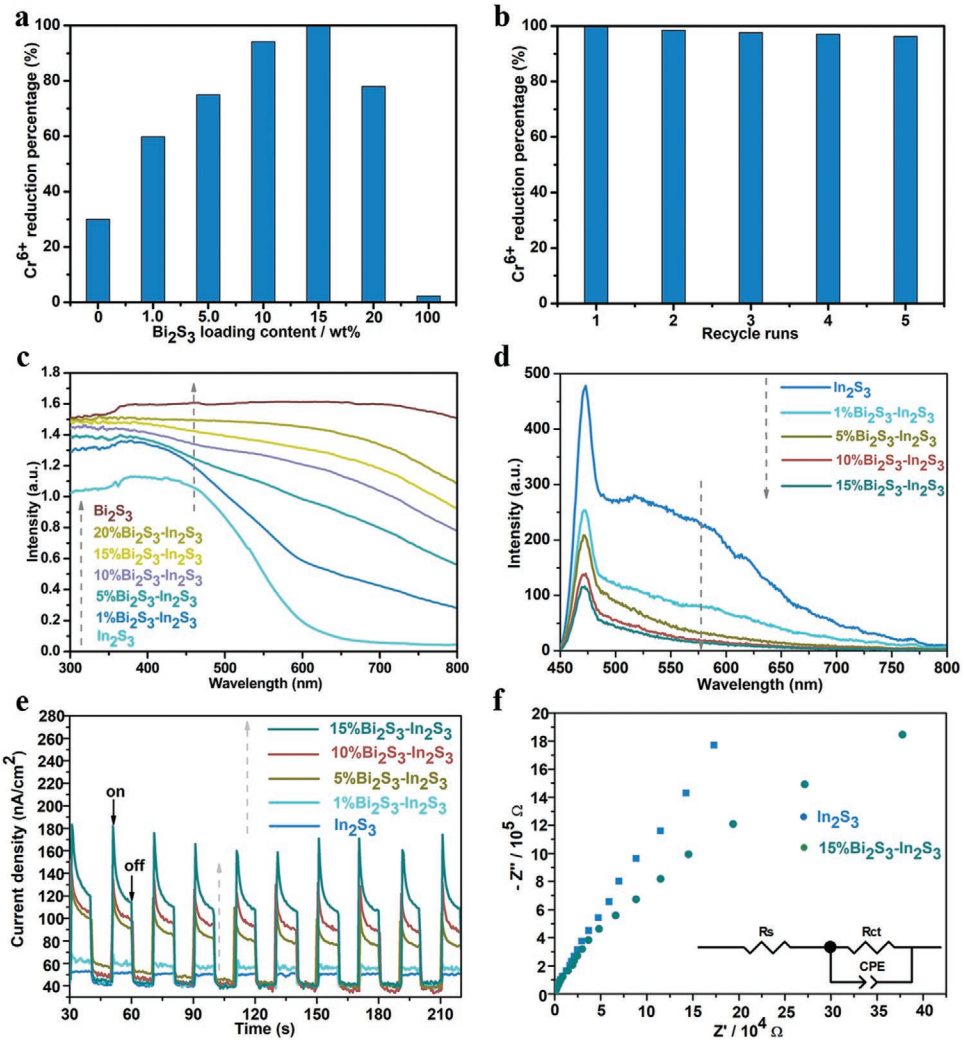

Figure 6. a) Photocatalytic activities of pristine In_2S_3, pristine Bi_2S_3, and Bi_2S_3–In_2S_3 heterostructures for Cr^{6+} removal. b) Photocatalytic activities of recycled Bi_2S_3–In_2S_3 heterostructures for Cr^{6+} reduction. c) DRS spectra, d) PL spectra. e) Instantaneous photocurrent densities of pristine In_2S_3, Bi_2S_3, and Bi_2S_3–In_2S_3 heterostructure samples with different Bi_2S_3 loading. f) Electrochemical impedance spectroscopy of pristine In_2S_3 and 15% Bi_2S_3–In_2S_3 samples.

2.4. Electron Transfer Pathways and Photocatalytic Mechanism

Electron spin resonance (ESR) measurement was carried out to examine the photogenerated electron transfer pathways as shown in **Figure 7**. The $\bullet O_2^-$ was trapped and established by 5,5-dimethyl-1-pyrroline-N-oxide (DMPO) reagent. After irradiation under visible light for 6 min, characteristic peaks related to $\bullet O_2^-$ signal were detected from In_2S_3 sample. In comparison,

Table 1. Comparison of the reaction conditions and photocatalytic efficiency achieved in this work with that of the previously reported literature.

Catalyst	Catalyst weight [mg mL^{-1}]	Cr concentration [mg L^{-1}]	Time [min]	Efficiency (%)	Refs.
TiO_2/Nd	250	10	180	99	[36]
TiO_2	10	10	50		[3]
MOF/Zn	1	10	330		[11]
ZrO_2-CuO	1	20	30	80	[1]
$Gd(OH)_3$/RGO	1	10	120	83	[6]
$BiWO_6$-Bi_2S_3	1	10	60	88	[37]
RGO/αFeOOH	1	10	180	94	[38]
Bi_2S_3-In_2S_3	0.2	20	< 30	100	This work

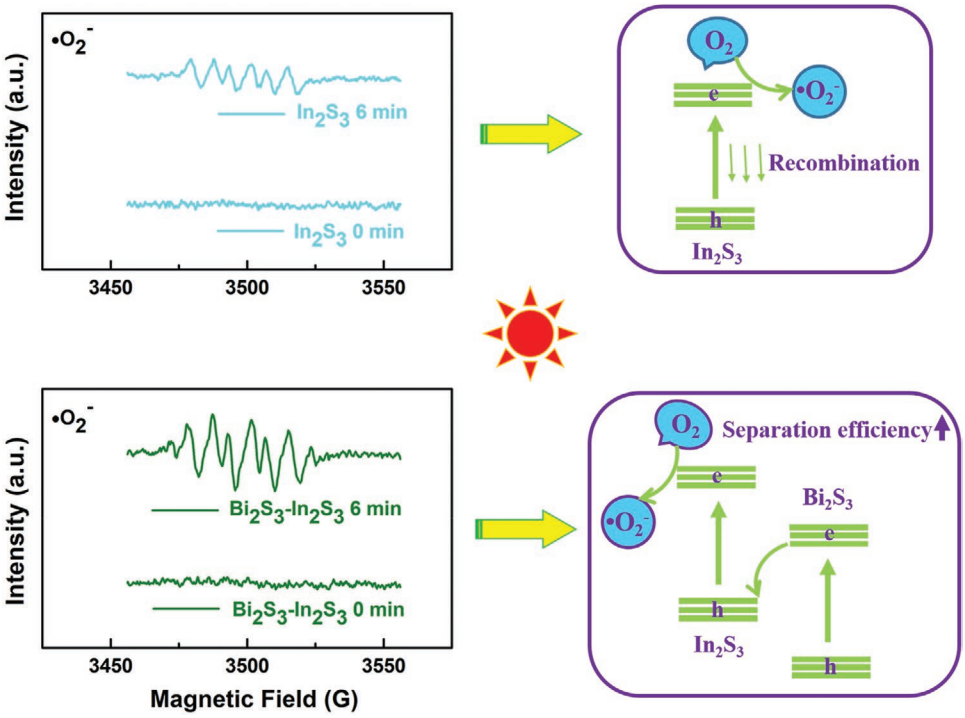

Figure 7. ESR spectrum of the $\bullet O_2^-$ produced by In_2S_3 and Bi_2S_3–In_2S_3 under visible-light irradiation.

Bi_2S_3–In_2S_3 heterostructure sample exhibits characteristic peaks of $\bullet O_2^-$ signal with much higher intensity than that of pristine In_2S_3. The conduction band of Bi_2S_3 is 0.4 eV which is more positive than the reaction energy potential of $O_2/\bullet O_2^-$ (-0.33 eV), so the electrons from the conduction band of Bi_2S_3 are more likely to directly transfer to the valence band of In_2S_3. Therefore, the $\bullet O_2^-$ are likely produced from the conduction band of In_2S_3 on the Bi_2S_3–In_2S_3 heterostructure. Due to a quick consumption of the photogenerated holes in In_2S_3, the charge carrier separation efficiency could be greatly improved, as evidenced by a higher $\bullet O_2^-$ intensity.

Based on the above result, the possible charge transfer mechanism of Bi_2S_3–In_2S_3 heterostructure for Cr^{6+} reduction is proposed. As shown in **Figure 8**a, In_2S_3 and Bi_2S_3 can both be excited under visbile-light illumination, the electrons on the conduction band of In_2S_3 can transfer to the conduction band of Bi_2S_3, following a type II p–n heterojunction scheme. However, the electrons on the conduction band of Bi_2S_3 do not produce $\bullet O_2^-$, as per the ESR result. So type II p–n heterojunction charge transfer is unlikely for the Bi_2S_3–In_2S_3 system. As per Z-scheme heterojunction shown in Figure 8b, electrons from the conduction band of Bi_2S_3 directly transfer to the valence band of In_2S_3, resulting in a higher charge carrier separation efficiency for In_2S_3, thereby also generating a higher $\bullet O_2^-$ intensity as confirmed by the ESR experiment and a higher photocatalytic activity. Thus, we can conclude that the Z-scheme mechanism exists in the Bi_2S_3–In_2S_3 heterojunction photocatalysts. Figure 8c shows the schematic illustration of both atomic level interface structure and the photocatalytic mechanism. The (060) crystal facet of Bi_2S_3 bonds with (440) crystal facet of In_2S_3 based on the HRTEM, lattice parameters of crystal structures of In_2S_3 and Bi_2S_3, XRD, and XPS analyses. The electrons from the conduction band of Bi_2S_3 transfer to the valance band of In_2S_3 via (060) crystal facet of Bi_2S_3 to (440) crystal facet of In_2S_3 forming a Z-scheme mechanism.

3. Conclusion

Facet-coupling Z-scheme Bi_2S_3–In_2S_3 nanoheterostructure photocatalysts with a series of loading ratios of Bi_2S_3 to In_2S_3 were fabricated through a facile one-pot hydrothermal method for photocatalytic Cr^{6+} reduction. We investigated microstructure, morphology, photocatalytic performance, and charge transfer mechanism of the photocatalysts through a systematic study utilizing multiple characterization techniques. The HRTEM, XRD, and XPS analyses revealed an intimate bonding between the (440) crystal facet of In_2S_3 and (060) crystal facet of Bi_2S_3, which provides a robust interface for efficient charge carrier transfer. On the other hand, the band structure alignments and the ESR traping experiment demonstrated that the charge carrier separation mechanism in the Bi_2S_3–In_2S_3 follows a Z-scheme pattern which is highly beneficial to improve the electron–hole separation efficiency and maintain a strong redox ability. The PL, photocurrent, and EIS analyses proved that the heterojunction photocatalyst presents a much-improved charge carrier separation efficiency than the pristine In_2S_3. A remarkable Cr^{6+} photoreduction activity was achieved for 15% Bi_2S_3–In_2S_3 heterostructure with 100% reduction within 30 min under a controlled amount of catalyst, which is around 3 and 44 times higher compared with pristine In_2S_3 and Bi_2S_3. These results confirm a great potential of Bi_2S_3–In_2S_3 heterostructures developed in this work for application in photocatalytic reduction of Cr^{6+}.

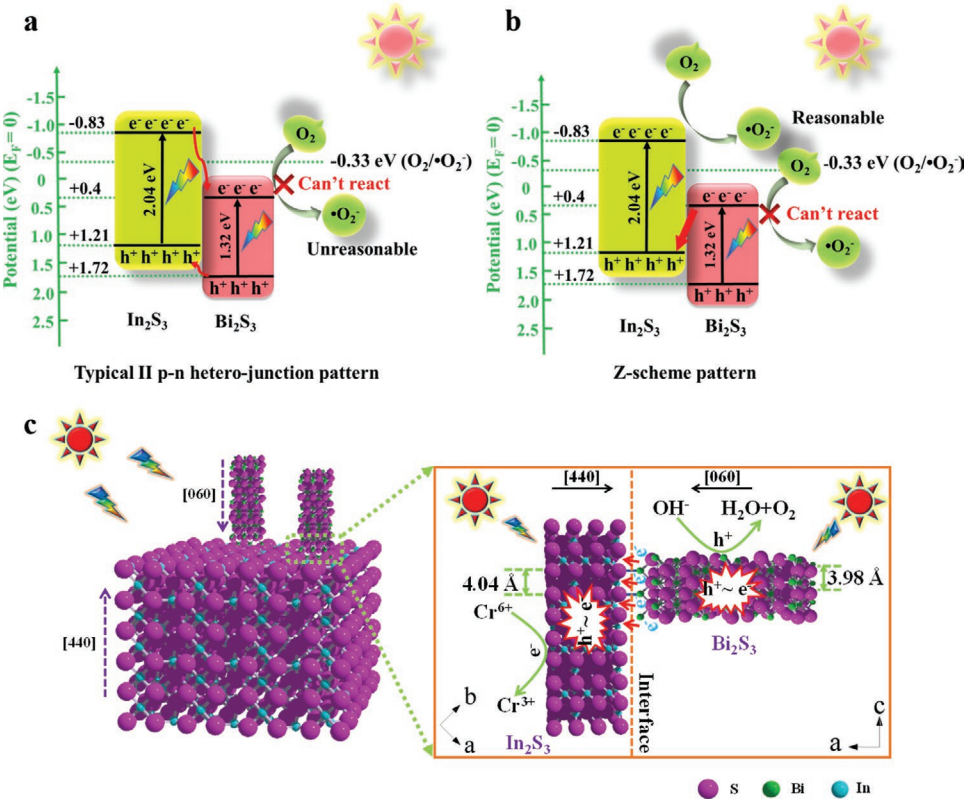

Figure 8. The proposed charge transfer pathways of a) Type II heterojunction and b) Z-scheme structure photocatalysts. c) Schematic illustration of the atomic structure and photocatalytic mechanism of Z-scheme Bi_2S_3–In_2S_3 photocatalyst for Cr^{6+} photoreduction.

4. Experimental Section

Reagents and Chemicals: All the reagents were purchased from commercial sources and utilized as received without further treatment. Indium acetate was obtained from Aladdin Reagent Co. Ltd. Bismuth nitrate pentahydrate and thioacetamide were purchased from Sinopharm Chemical Reagent Co. Ltd., China. Ultra-purified water (18.25 Mπ cm) was used in aqueous solution preparations.

Synthesis of In_2S_3, Bi_2S_3, and Bi_2S_3–In_2S_3 Nanostructures: The In_2S_3 nanostructures were synthesized as reported in the literature. Typically, a precise amount of indium acetate precursor was added into 40 mL of water until fully dissolved. Then a relative amount of thioacetamide was slowly added into the solution with continuous stirring until the solution turns transparent. The mixture was transferred into a 100 mL autoclave and heated at 200 °C for 24 h. After cooling the autoclave, the synthesized products were separated by centrifugation, followed by repeated washing with water and ethanol. Finally, the products were collected for further use after drying at 80 °C.

The Bi_2S_3–In_2S_3 nanostructures with different ratios of Bi_2S_3 were synthesized following a procedure similar to that of In_2S_3 synthesis. Typically, a certain amount of $In(CH_3COO)_3$ and a varying amount of bismuth nitrate pentahydrate were dissolved in 40 mL water under constant stirring. Consecutively, an excessive amount of TAA was dissolved in the solution. After complete dissolution, the mixture was transferred into a 100 mL autoclave and heated at 200 °C for 24 h. The Bi_2S_3 nanostructures were also prepared following the same procedure except for the addition of $In(CH_3COO)_3$.

Material Characterizations: To investigate the crystal structure of the synthesized samples, XRD patterns were obtained by Rigaku Miniflex 600 with Cu Kα1 radiation (λ = 0.154178 nm) at 40 kV and 40 mA. The morphology and microstructural characterizations were performed by FESEM analysis conducted using Zeiss SIGMA FESEM with an accelerating voltage of 20 kV. Further morphology and lattice fringe information were obtained by transmission electron microscope (TEM) and high-resolution transmission electron microscope conducted using JEM-2100 TEM with an accelerating voltage of 200 kV. The elemental composition and band energy information were obtained by XPS characterization conducted using ESCALAB250Xi (Thermo Fisher Scientific) with an Mg Kα X-ray source, and the spectra were adjusted to the C 1s peak at 284.8 eV.

Optical and Electrochemical Characterizations: The DRS for different photocatalyst samples were obtained by a Shimadzu UV-3600 spectrometer using $BaSO_4$ as a reference. The charge carrier separation efficiency was evaluated by PL spectra measured by Hitachi F-4500 luminescence spectrometer. Electron transfer efficiency at the interface was characterized by transient photocurrent curves and EIS conducted using CHI 660E electrochemical analyzer in a standard three-electrode configuration. Na_2SO_4 solution (0.5 M) was used as the electrolyte while saturated calomel electrode (SCE), glassy carbon electrode, and Pt plate were used as the reference, working, and counter electrodes, respectively. The working electrode was prepared by depositing catalyst Nafion suspension solution (100 µL, 2.0 g L^{-1}) on fluorine-doped tin oxide (FTO) coated glass (1 cm^2), which was dried at 60 °C for 2 h.

Photocatalytic Activity Evaluation: In a typical experiment to measure the photocatalytic efficiency for Cr^{6+} removal, 15 mg catalyst was placed into 75 mL Cr^{6+} solution with 20 ppm concentration and the solution was irradiated by 300 W Xe lamp with a 420 nm cutoff filter. $H_2Cr_2O_7$ was used as the source of Cr^{6+} to prepare the Cr^{6+} solution. The mixture was ultrasonicated for 5 min and stirred for 30 min before irradiation. After every 30 min irradiation interval, 5 mL of liquid was collected from the reactor for further analysis. Any suspended photocatalyst materials were filtered out by centrifugation. 1 mL of the collected solution was further diluted to 50 mL and then added with 2.5 mL chromogenic reagent. The absorption intensity was measured by a UV–vis spectrophotometer (UV-3600) at 540 nm.

The concentration of Cr^{6+} before and after photocatalytic reduction was determined using a chromogenic agent and a standard curve. The chromogenic agent was prepared using the following procedure: 0.2 g of diphenylcarbazide (DCP) was dissolved in 100 mL of 95% ethanol, followed by the addition of 1:9 vol% H_2SO_4:H_2O into the solution under vigorous stirring until the DCP dissolves fully. A standard curve (concentration vs absorbance) was obtained by dissolving known amounts of $H_2Cr_2O_7$ in water and quantifying their respective absorbance. To detect the Cr^{6+} concentration of the samples from photoreduction experiments, the absorbance of the samples was measured and compared against the standard curve. It is noted that Cr^{6+} reduces to Cr^{3+} which dissolves in the solution. The chromogenic agent selectively reacts with Cr^{6+}, so the measured absorption intensity is directly ascribable to the reduction of Cr^{6+}.

Supporting Information

Supporting Information is available from the Wiley Online Library or from the author.

Acknowledgements

This work was supported by the National Natural Science Foundation of Jiangsu Province (BK20151248), the Large-scale Instrument Equipment Sharing Foundation of Wuhan University, and the Australian Renewable Energy Agency. The authors acknowledge Analytical and Testing Center of Wuhan University. The authors also thank the Center for Electron Microscopy at Wuhan University.

Conflict of Interest

The authors declare no conflict of interest.

Data Availability Statement

The data that support the findings of this study are available from the corresponding author upon reasonable request.

Keywords

1D–0D nanostructure, Bi_2S_3–In_2S_3 heterojunction, Cr^{6+} removal, facet coupling, visible-light-driven, Z-scheme photocatalyst

Received: March 29, 2021
Revised: July 20, 2021
Published online:

[1] B. Nanda, A. C. Pradhan, K. M. Parida, *Chem. Eng. J.* **2017**, *316*, 1122.
[2] a) C. Yu, P. Yang, L. Tie, S. Yang, S. Dong, J. Sun, J. Sun, *Appl. Surf. Sci.* **2018**, *455*, 438; b) V. Balakumar, H. Kim, R. Manivannan, H. Kim, J. W. Ryu, G. Heo, Y.-A. Son, *Ultrason. Sonochem.* **2019**, *59*, 104738.
[3] C. Athanasekou, G. E. Romanos, S. K. Papageorgiou, G. K. Manolis, F. Katsaros, P. Falaras, *Chem. Eng. J.* **2017**, *318*, 171.
[4] a) N. Song, M. Zhang, H. Zhou, C. Li, G. Liu, S. Zhong, S. Zhang, *Appl. Surf. Sci.* **2019**, *495*, 143551; b) Z. Lv, H. Zhou, H. Liu, B. Liu, M. Liang, H. Guo, *Chem. Eng. J.* **2017**, *330*, 1297.
[5] H. He, Z. Luo, Z.-Y. Tang, C. Yu, *Appl. Surf. Sci.* **2019**, *490*, 460.
[6] D. k. Padhi, G. K. Pradhan, K. M. Parida, S. K. Singh, *Chem. Eng. J.* **2014**, *255*, 78.
[7] a) N. Zhang, G. Li, S. Wang, X. Xu, L. Li, *Catal. Commun.* **2019**, *119*, 129; b) Y. Lu, J. Song, W. Li, Y. Pan, H. Fang, X. Wang, G. Hu, *Appl. Surf. Sci.* **2020**, *506*, 145000; c) J. Sun, Z. Zhang, J. Ji, M. Dou, F. Wang, *Appl. Surf. Sci.* **2017**, *405*, 372; d) J. Hu, P. Tao, S. Wang, Y. Liu, Y. Tang, H. Zhong, Z. Lu, *J. Mater. Chem. A* **2013**, *1*, 6558.
[8] a) Q. Cai, C. Liu, C. Yin, W. Huang, L. Cui, H. Shi, X. Fang, L. Zhang, S. Kang, Y. Wang, *ACS Sustainable Chem. Eng.* **2017**, *5*, 3938; b) C. Shi, H. Qi, Z. Sun, K. Qu, Z. Huang, J. Li, M. Dong, Z. Guo, *J. Mater. Chem. C* **2020**, *8*, 2238; c) R. Vinu, G. Madras, *Environ. Sci. Technol.* **2008**, *42*, 913.
[9] V. Kostas, M. Baikousi, K. Dimos, K. C. Vasilopoulos, I. Koutselas, M. A. Karakassides, *J. Phys. Chem. C* **2017**, *121*, 7303.
[10] C. Liu, X. Cui, Y. Li, Q. Duan, *Chem. Eng. J.* **2020**, *399*, 125807.
[11] Q.-Q. Xu, H.-J. Fan, Y.-T. Li, K. E. Christensen, T.-z. Ren, *Polyhedron* **2015**, *92*, 60.
[12] L. Wang, S. K. Karuturi, L. Zan, *Appl. Surf. Sci.* **2021**, *537*, 148063.
[13] a) Q. Xu, L. Zhang, J. Yu, S. Wageh, A. A. Al-Ghamdi, M. Jaroniec, *Mater. Today* **2018**, *21*, 1042; b) Z. Zhang, W. Wang, L. Wang, S. Sun, *ACS Appl. Mater. Interfaces* **2012**, *4*, 593.
[14] a) L. Meng, J. He, W. Tian, M. Wang, R. Long, L. Li, *Adv. Energy Mater.* **2019**, *9*, 1902135. b) E. Hua, S. Jin, X. Wang, S. Ni, G. Liu, X. Xu, *Appl. Catal., B* **2019**, *245*, 733.
[15] a) L. Wang, B. Zhao, C. Wang, M. Sun, Y. Yu, B. Zhang, *J. Mater. Chem. A* **2020**, *8*, 10175. b) S. Wang, B. Y. Guan, Y. Lu, X. W. D. Lou, *J. Am. Chem. Soc.* **2017**, *139*, 17305.
[16] H. Xu, Y. Wang, X. Dong, N. Zheng, H. Ma, X. Zhang, *Appl. Catal., B* **2019**, *257*, 117932.
[17] a) Z. Li, Z. Zhou, J. Ma, Y. Li, W. Peng, G. Zhang, F. Zhang, X. Fan, *Appl. Catal., B* **2018**, *237*, 288; b) L. Xu, Q. Jiang, Z. Xiao, X. Li, J. Huo, S. Wang, L. Dai, *Angew. Chem., Int. Ed.* **2016**, *55*, 5277.
[18] T. Yan, J. Tian, W. Guan, Z. Qiao, W. Li, J. You, B. Huang, *Appl. Catal., B* **2017**, *202*, 84.
[19] Z. Wu, X. Yuan, G. Zeng, L. Jiang, H. Zhong, Y. Xie, H. Wang, X. Chen, H. Wang, *Appl. Catal., B* **2018**, *225*, 8.
[20] B. Shao, X. Liu, Z. Liu, G. Zeng, Q. Liang, C. Liang, Y. Cheng, W. Zhang, Y. Liu, S. Gong, *Chem. Eng. J.* **2019**, *368*, 730.
[21] M. Chahkandi, M. Zargazi, *J. Hazard. Mater.* **2019**, *380*, 120879.
[22] Y. Chen, G. Tian, Q. Guo, R. Li, T. Han, H. Fu, *CrystEngComm* **2015**, *17*, 8720.
[23] J. Zhou, G. Tian, Y. Chen, Y. Shi, C. Tian, K. Pan, H. Fu, *Sci. Rep.* **2014**, *4*, 4027.
[24] a) W. Dong, D. Wang, H. Wang, M. Li, F. Chen, F. Jia, Q. Yang, X. Li, X. Yuan, J. Gong, H. Li, J. Ye, *J. Colloid Interface Sci.* **2019**, *535*, 444; b) R. Wu, Y. Xu, R. Xu, Y. Huang, B. Zhang, *J. Mater. Chem. A* **2015**, *3*, 1930.
[25] a) Y. Guo, Y. Ao, P. Wang, C. Wang, *Appl. Catal., B* **2019**, *254*, 479; b) C. Zhuang, L. Tang, Z. Yu, T. Peng, Y. Zhang, L. Li, Y. Zhou, Z. Zou, *Catal. Sci. Technol.* **2019**, *9*, 182; c) X. Xu, L. Meng, Y. Li, C. Sun, S. Yang, H. He, *Appl. Surf. Sci.* **2019**, *479*, 410; d) C. Zhang, W. Wang, M. Zhao, J. Zhang, Z. Zha, S. Cheng, H. Zheng, H. Qian, *J. Colloid Interface Sci.* **2019**, *546*, 303.
[26] L. Ye, J. Liu, Z. Jiang, T. Peng, L. Zan, *Appl. Catal., B* **2013**, 142, *1*.
[27] a) C. Xing, Z. Wu, D. Jiang, M. Chen, *J. Colloid Interface Sci.* **2014**, *433*, 9; b) M.-Q. Yang, B. Weng, Y.-J. Xu, *J. Mater. Chem. A* **2014**, *2*, 1710; c) X. Zhang, N. Zhang, C. Gan, Y. Liu, L. Chen, C. Zhang, Y. Fang, *Mater. Sci. Semicond. Process.* **2019**, *91*, 212.
[28] a) Y. Zhang, W. Gao, S. Ji, D. Zhao, X. Bai, H. Xue, N. Jia, *Electrochim. Acta* **2019**, *320*, 134619; b) H. Sun, Z. Jiang, D. Wu, L. Ye, T. Wang, B. Wang, T. An, P. K. Wong, *ChemSusChem* **2019**, *12*, 890; c) A. Chachvalvutikul, W. Pudkon, T. Luangwanta, T. Thongtem, S. Thongtem, S. Kittiwachana, S. Kaowphong, *Mater. Res. Bull.* **2019**, *111*, 53.
[29] K. Ghosh, S. K. Srivastava, *Dalton Trans.* **2020**, *49*, 16993.

[30] N. Song, M. Zhang, H. Zhou, C. Li, G. Liu, S. Zhong, S. Zhang, *Appl. Surf. Sci.* **2019**, *143551*, 495.
[31] R. Peng, Y. Ma, S. Zhang, B. Huang, L. Kou, Y. Dai, *Mater. Horiz.* **2020**, *7*, 504.
[32] A. Helal, F. A. Harraz, A. A. Ismail, T. M. Sami, I. A. Ibrahim, *Mater. Des.* **2016**, *102*, 202.
[33] Z. Zhang, C. Zhou, L. Huang, X. Wang, Y. Qu, Y. Lai, J. Li, *Electrochim. Acta* **2013**, *114*, 88.
[34] X. Chen, W. Zhang, L. Zhang, L. Feng, J. Wen, J. Yang, C. Zhang, J. Jiang, H. Wang, *Appl. Surf. Sci.* **2019**, *481*, 1335.
[35] Q.-Y. Tang, R. Huo, L.-Y. Ou, X.-L. Luo, Y.-R. Lv, Y.-H. Xu, *Chin. J. Catal.* **2019**, *40*, 580.
[36] S. Rengaraj, S. Venkataraj, J.-W. Yeon, Y. Kim, X. Z. Li, G. K. H. Pang, *Appl. Catal., B* **2007**, *77*, 157.
[37] A. Rauf, M. S. A. Sher Shah, G. H. Choi, U. B. Humayoun, D. H. Yoon, J. W. Bae, J. Park, W.-J. Kim, P. J. Yoo, *ACS Sustainable Chem. Eng.* **2015**, *3*, 2847.
[38] D. K. Padhi, K. Parida, *J. Mater. Chem. A* **2014**, *2*, 10300.
[39] Y. Gao, S. Zhang, X. Bu, Y. Tian, *Catal. Today* **2019**, *327*, 271.
[40] J. Xu, L. Zhang, R. Shi, Y. Zhu, *J. Mater. Chem. A* **2013**, *1*, 14766.